J Solid State Electrochem (2013) 17:1479–1485
DOI 10.1007/s10008-013-2026-2

ORIGINAL PAPER

Nitridated mesoporous $Li_4Ti_5O_{12}$ spheres for high-rate lithium-ion batteries anode material

Yunyan Zhao · Shuping Pang · Chuanjian Zhang · Qinghua Zhang · Lin Gu · Xinhong Zhou · Guicun Li · Guanglei Cui

Received: 23 December 2012 / Revised: 28 January 2013 / Accepted: 29 January 2013 / Published online: 10 February 2013

Abstract Nitridated mesoporous $Li_4Ti_5O_{12}$ spheres were synthesized by a simple ammonia treatment of $Li_4Ti_5O_{12}$ derived from mesoporous TiO_2 particles and lithium acetate dihydrate via a solid state reaction in the presence of polyethylene glycol 20000. The carbonization of polyethylene glycol could effectively restrict the growth of primary particles, which was favorable for lithium ions diffusing into the nanosized TiO_2 lattice during the solid state reaction to form a pure phase $Li_4Ti_5O_{12}$. After a subsequent thermal nitridation treatment, a high conductive thin TiO_xN_y layer was in situ constructed on the surface of the primary nanoparticles. As a result, the nitridated mesoporous $Li_4Ti_5O_{12}$ structure, possessing shorter lithium-ion diffusion path and better electrical conductivity, displays significantly improved rate capability. The discharge capacity reaches 138 $mAhg^{-1}$ at 10 C rate and 120 $mAhg^{-1}$ at 20 C rate in the voltage range of 1–3 V.

Keywords Nitridated mesoporous $Li_4Ti_5O_{12}$ spheres · Ammonia treatment · Mesoporous TiO_2 · Polyethylene glycol 20000 · TiO_xN_y layer

Introduction

Rechargeable lithium-ion batteries (LIBs) with both high-power and high-energy densities are excellent power sources for portable electronic devices and electric vehicles [1–3]. For the commercial LIBs, graphite as the anode material suffers from low-rate performance due to its low lithium diffusion coefficient and thus failing to meet the requirement in high-power applications [4].

$Li_4Ti_5O_{12}$ (LTO) is rational to be a kind of long lifetime and safe anode material owing to its zero-strain insertion crystal structure [5, 6]. However, its intrinsic electrical conductivity (ca. $10^{-13}\,Scm^{-1}$) and lithium-ion diffusion coefficient (ca. 10^{-9}–$10^{-13}\,cm^2s^{-1}$) are relatively low and prohibitive for achieving high-rate performance [7, 8]. In order to realize the high-power application, many efforts have been made to ameliorate the lithium-ion diffusion and electron transfer efficiency, including doping with foreign atoms [9–11], synthesizing nanostructures [12–16], and introducing electronically conductive coatings [17–20]. Synthesizing nanostructured LTO particles or sheets is one of the most efficient strategies to reduce the lithium-ion diffusion and electron transport pathway so as to improve their rate capability [12, 13]. Unfortunately, downsizing the LTO particle to the nanoscale inevitably diminishes the powder tap density and volumetric energy density of the cell [21, 22]. Mesoporous material, assembled with well-crystalline nanoparticles, is an ideal structure to resolve the above-mentioned problems and still can keep a favorable electrode–electrolyte interface for the rapid lithium-ion diffusion [23, 24]. The key challenge is the construction of an

Electronic supplementary material The online version of this article (doi:10.1007/s10008-013-2026-2) contains supplementary material, which is available to authorized users.

Yunyan Zhao and Shuping Pang contributed equally to this work.

Y. Zhao · X. Zhou · G. Li (✉)
Qingdao University of Science and Technology, Qingdao 266042, People's Republic of China
e-mail: guicunli@qust.edu.cn

Y. Zhao · S. Pang · C. Zhang · G. Cui (✉)
Qingdao Key Lab of Solar Energy Utilization and Energy Storage Technology, Qingdao Institute of Bioenergy and Bioprocess Technology, Chinese Academy of Sciences, Qingdao 266101, People's Republic of China
e-mail: cuigl@qibebt.ac.cn

Q. Zhang · L. Gu
Beijing National Laboratory for Condensed Matter Physics, The Institute of Physics, Chinese Academy of Sciences, Beijing 100190, People's Republic of China

efficient conducting pathway in such structure to quickly transfer electrons throughout the mesoporous spheres [21, 22]. In this case, carbon- or nitrogen-doped carbon layers have been prepared on the surface of LTO by carbonizing organic precursors, such as pitch, sugar, ionic liquid 1-ethyl-3-methylimidazolium dicyanamide, and urea, to enhance their electrical conductivity [21, 22, 25, 26]. However, there is no doubt that the electrical conductivity of such kind of coating prepared by high-temperature (800 °C) pyrolysis is still relatively low.

Whereas, it has been recently reported that the nitridation of the Ti-based compounds (TiO_2 and LTO) can form a more conductive TiO_xN_y species [27–31]. Motivated by this, herein, a simple ammonia treatment was applied to form thin TiO_xN_y layers covered on the primary nanoparticles' surface of the mesoporous LTO spheres to improve their whole electrical conductivity. It was measured that the conductivity of TiO_xN_y film generated with an ammonia treatment is about 565 Scm^{-1}, which is much higher than that of the carbon layers (~50 Scm^{-1} with polyethylene glycol 20000 as the carbon source). As a result, the lithium battery fabricated with the as-prepared nitridated mesoporous $Li_4Ti_5O_{12}$ spheres (LTO-N) exhibits significantly improved rate capability, and the discharge capacity reaches 138 $mAhg^{-1}$ at 10 C rate and 120 $mAhg^{-1}$ at 20 C rate.

Experimental

Synthesis of mesoporous TiO_2 spheres

All reagents were used as received without further purification. The mesoporous TiO_2 spheres were prepared as reported by Zhong and co-workers [32]. Firstly, 6.0 mL butyl titanate was dissolved in 150.0 mL ethylene glycol and stirred for 8 h. Then, the solution was poured into a 518.1-mL mixed solution which contained acetone and deionized water with a volume ratio of 340:1. Secondly, the obtained white precursor was refluxed with water at 100 °C for 2 h to form the mesoporous TiO_2 spheres. The precipitate was separated by centrifugation and washed with deionized water and ethyl alcohol for several times and then dried at 60 °C for 3 h.

Synthesis of carbon-coated mesoporous LTO (LTO-C) spheres

A 0.500 g mesoporous TiO_2, 0.595 g lithium acetate dihydrate, and 0.115 g polyethylene glycol 20000 (PEG 20000) as a carbon source were mixed in 20.0 mL alcohol and stirred at 70 °C for 1 h, followed by drying overnight at 80 °C. Then, this mixture was annealed at 800 °C for 20 h under N_2 atmosphere to gain LTO-C spheres.

Synthesis of nitridated mesoporous LTO (LTO-N) spheres

The LTO-N was prepared by a thermal treatment of mesoporous LTO-C spheres in NH_3 atmosphere at 700 °C for 1 h. The heating rate was 5 °C min^{-1}, and the cooling rate is 3 °C min^{-1}.

Material characterization

The phase composition of the samples was characterized using X-ray diffraction (XRD, Bruker-AXS Microdiffractometer D8 Advance) with Cu Ka radiation (λ=1.5406 Å) from 10 to 80°. The morphology of the synthesized materials was observed using a field-emission scanning electron microscopy (Hitachi S-4800) and a transmission electron microscope (TEM; JEOL 2100-F). The high-resolution transmission electron microscopy (HRTEM) image, high-angle annular dark-field scanning transmission electron microscopy (HAADF-STEM) image, and element analysis mapping were carried out on a JEOL JEM-2010 (HR) electron microscope operated at 200 kV. The content of coated carbon in $Li_4Ti_5O_{12}$ sample was determined by a Rubotherm-DynTHERM-HP thermal analyser. The X-ray photoelectron spectroscopy (XPS) was obtained using an ESCALab220i-XL spectrometer (VG Scientific) with Al Kα radiation in twin anode at 14 kV×16 mA.

Electrochemical test

Electrochemical experiments were carried out using standard R2032-type coin cells assembled in an argon-filled glove box. The anodes were prepared by mixing 80 wt% active material, 10 wt% conductive carbon black, and 10 wt% poly(vinyl difluoride) with appropriate amount of *N*-methyl-2-pyrrolidone solvent. The slurry was cast on Cu foil to a thickness of approximately 70 μm and subsequently dried in a vacuum oven at 120 °C for 8 h to remove the residual solvent. Pure lithium foil was used as the counter electrode and separated by a Celgard 2500 membrane separator. The electrolyte solution was 1 M $LiPF_6$ in ethylene carbonate/dimethyl carbonate (1:1 by volume). Galvanostatical discharge–charge experiments were conducted over a voltage range of 1.0–3.0 V (vs. Li^+/Li) at different rates using a LAND battery testing system. Electrochemical impedance spectroscopy (EIS) measurements were carried out on a ZAHNER ZENNIUM electrochemical workstation by applying a sine wave with an amplitude of 5.0 mV over the frequency range from 100 kHz to 100 MHz. Cyclic voltammetry curves were performed using a CHI 440A instrument (CHI Instrument, Inc.) at a scanning rate of 0.2 mVs^{-1}. The conductivity is measured by a two-electrode method with 50-nm-thick

silver as the electrode. The channel length and width are 1 and 5 mm, respectively.

Results and discussion

Structure and morphology of materials

To synthesize mesoporous LTO, mesoporous TiO_2 spheres (300–500 nm) assembled with 10–20 nm primary nanoparticles were firstly obtained (see supporting information Fig. S1). After a solid state reaction with lithium acetate dihydrate, mesoporous LTO-C spheres were synthesized as illustrated in Fig. 1a, b. It is found that the presence of PEG 20000 in the synthesis process is critical to maintain the mesoporous structure and favorable for the lithium ions to diffuse into the nanosized TiO_2 particles to form a pure phase LTO (see XRD patterns in supporting information Fig. S2). After such a solid state reaction at 800 °C for 20 h, the organic PEG precursor was decomposed and carbonized to form a conductive layer on the surface of the primary nanoparticles [22]. The thermogravimetric test acquired in air from 20 °C to 800 °C is shown in Fig. S3. The weight loss happening at ~450 °C is attributed to the decomposition of the covered carbon layer in the air. The weight content of carbon within the LTO-C is estimated to be 5.2 wt%. After a subsequent nitridation of the LTO-C in NH_3 atmosphere at 700 °C for 1 h, the morphology and structure including the size of the primary nanoparticles do not change obviously as shown in Fig. 1c, d. Most importantly, the LTO crystalline phase is also well maintained after nitridation according to the X-ray diffraction patterns in Fig. S2.

As shown in the HRTEM image in Fig. 2a, it can be clearly observed that the primary particle of LTO is highly crystallized. The clear lattice fringe with a distance of 0.472 nm is consistent with the (111) atomic planes of the spinel LTO. In addition, the surface of individual primary particles was surrounded by a thin coating layer. A lattice fringe with a distance of 0.126 nm in this coating layer belongs to the TiO_xN_y phase, which is likely derived from the in situ formed during the thermal treatment under ammonia. Figure 2b exhibits HAADF-STEM image of LTO-N and the energy-dispersive X-ray (EDX) mapping images of C, N, and Ti elements. Mesoporous structure is clearly visible; furthermore, C, N, and Ti elements display the similar distribution, implying that both C and N elements are uniformly covered on the primary particles, which is consistent with the TEM results as shown in Fig. 1d.

To further investigate the surface composition of the LTO-N particles, XPS is carried out as shown in Fig. 3 (full spectrum is shown in Fig. S4). It can be observed that the

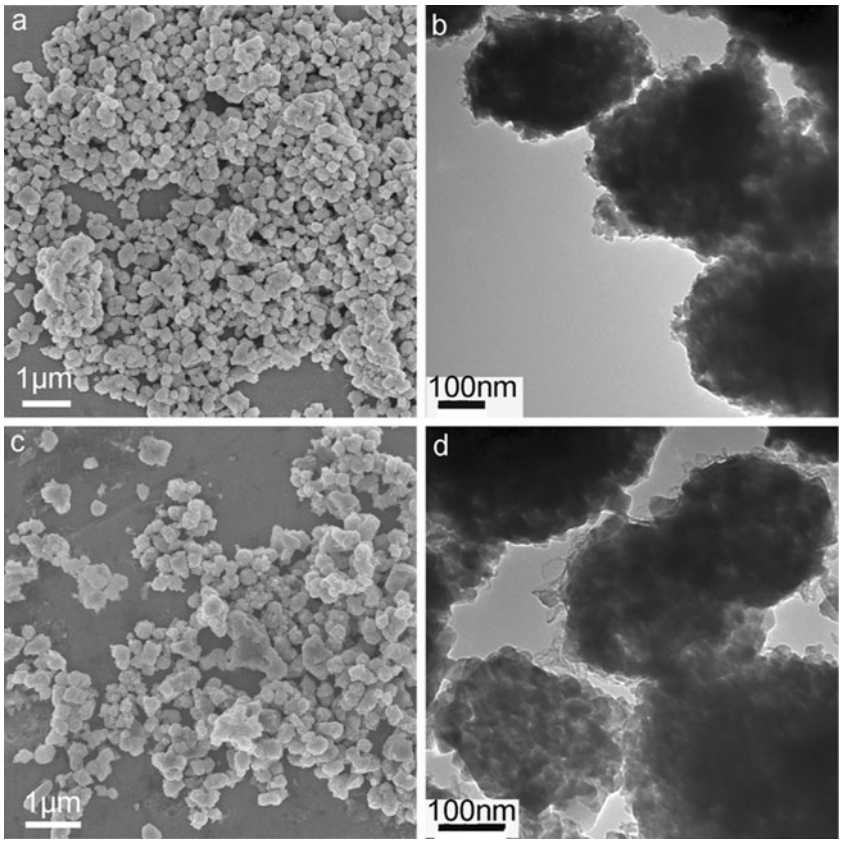

Fig. 1 **a** Typical SEM image of LTO-C. **b** Typical TEM image of LTO-C. **c** Typical SEM image of LTO-N. **d** Typical TEM image of LTO-N

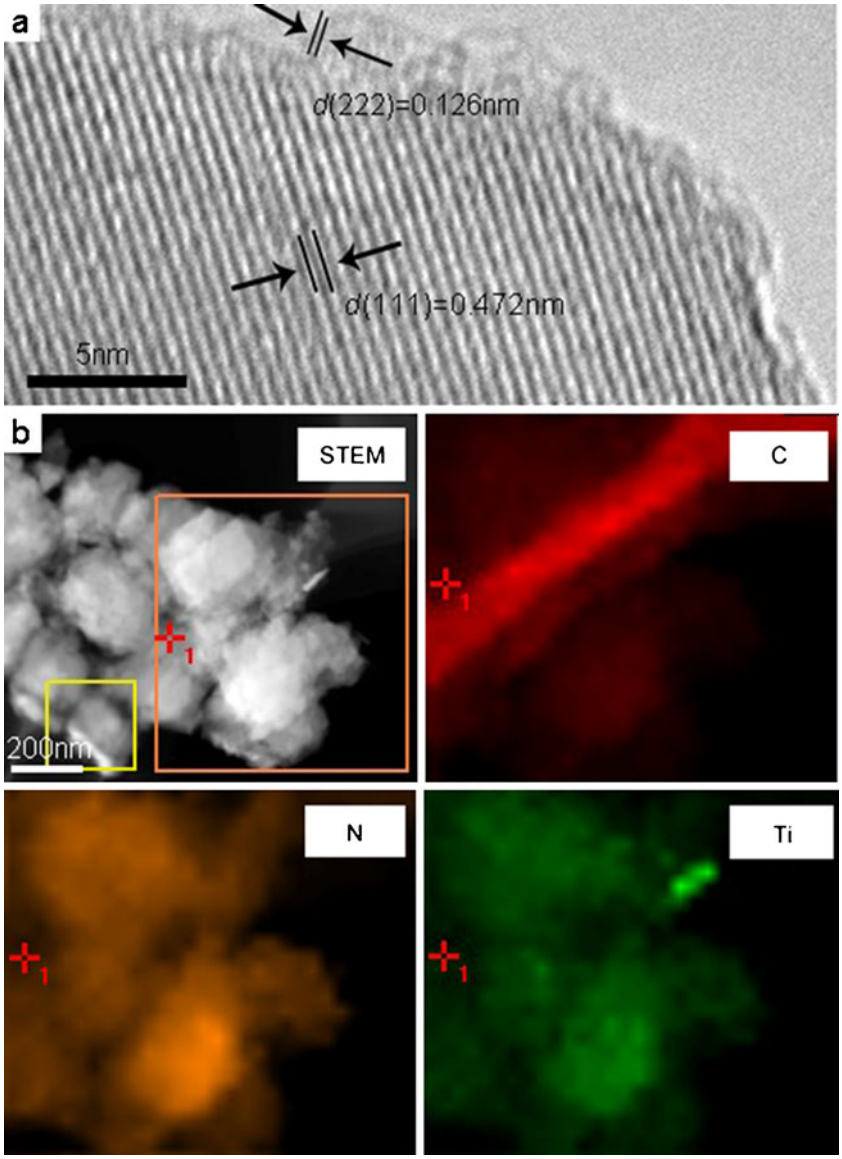

Fig. 2 **a** HRTEM image of LTO-N. **b** HAADF-STEM image of LTO-N and EDX mapping of C, N, and Ti elements

surface of LTO-N is made up of C, N, Ti, and O elements. Ti 2*p* peaks appear at 456.0 and 461.5 eV, which can be assigned to Ti^{3+} $2p_{3/2}$, and Ti^{3+} $2p_{1/2}$, respectively, implying the presence of Ti^{3+} in the LTO-N sample [33]. The existence of Ti^{3+} is consistent with the result of HRTEM image in Fig. 2. As Fig. 3b presents, the existence of multiple components in the spectrum of N 1*s* suggests that the coexistence of different chemical states of N. The N 1*s* peak is deconvoluted on three components: the peaks at binding energies of 397.6, 399.3, and 402.3 eV are ascribed to the Ti–N, C–N, and C=N bonds, respectively [25, 26, 34]. In addition, C≡N bond, whose binding energy is close to that of the C–N bond, might also

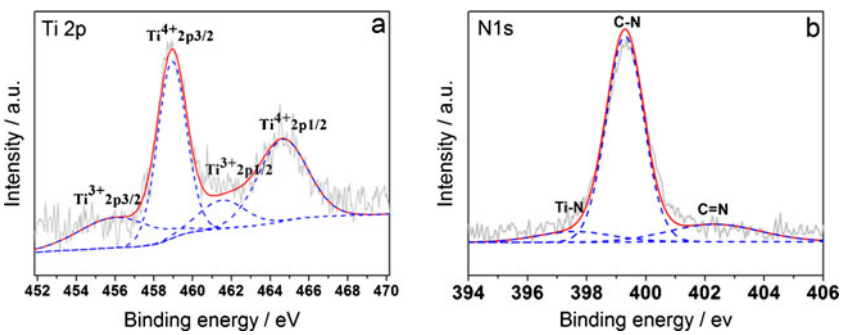

Fig. 3 **a** High-resolution XPS survey spectra of Ti 2*p* in LTO-N. **b** High-resolution XPS survey spectra of N 1*s* in LTO-N

exist [25]. Compared with the reported value 397.0 eV, the binding energy of N 1*s* in Ti–N bonds showed a small blueshift, which is due to the binding between Ti and O elements on the spheres surface [26].

Electrochemical performance

Figure 4 presents cyclic voltammograms of LTO-C and LTO-N measured at a scan rate of 0.2 mVs^{-1} within a potential window of 1–3 V (vs. Li/Li^{+}). The oxidation peaks (anodic delithiation) and the reduction peak (cathodic lithiation) represent the oxidation/reduction reactions of the Ti^{3+}/Ti^{4+} couple in the cubic structure, which reveals the behavior of lithium deinsertion–insertion processes in spinel LTO electrode [19, 35]. Insertion and extraction peaks of two samples are sharp and similar in intensity, which is decided by their similar morphology. The smaller primary particle size (10–20 nm) shortens the distance of lithium-ion diffusion in LTO particles, and the higher surface area of mesoporous spheres provides a higher electrode/electrolyte contact surface area which results in a low electrochemical reaction resistance during the charge/discharge process and good electrode kinetic process. The voltage difference of the LTO-N cell between anodic and cathodic peaks is 0.16 V, obviously much smaller than that of LTO-C electrode. The alleviated polarization implies an augment of the mixed (ionic and electronic) conductivity after the nitridation treatment, indicating that there is a favorable interfacial performance [36] and better electrical conductivity in the as-prepared mesoporous LTO-N spheres.

The enhancement of the electrical conductivity is further proved by the electrochemical impedance spectroscopy measurements as given in Fig. 5. By fitting of the experimental results, the equivalent circuit (the inset in Fig. 5) was employed because it has least deviation. According to the literatures [9, 37, 38], an intercept at the Z' real axis in the high frequency represents to the resistance of the electrolytes (R_s), which is 72 and 9.17Ω for LTO-C and LTO-N, respectively. The depressed semicircle at high-middle frequency is associated with the charge transfer resistance (R_{ct}), which corresponds to 450 and 150Ω for LTO-C and LTO-N, respectively. CPE is the corresponding constant phase element. Also, the sloping line in the low frequency is related to Warburg impedance (Z_w), which is related to the solid-state diffusion of lithium ions into the anode material. The LTO-N nanocomposite electrode exhibits much smaller charge transfer resistance than that of the LTO-C, demonstrating that thermal nitridation is indeed a favorable approach to enhance the electrical conductivity.

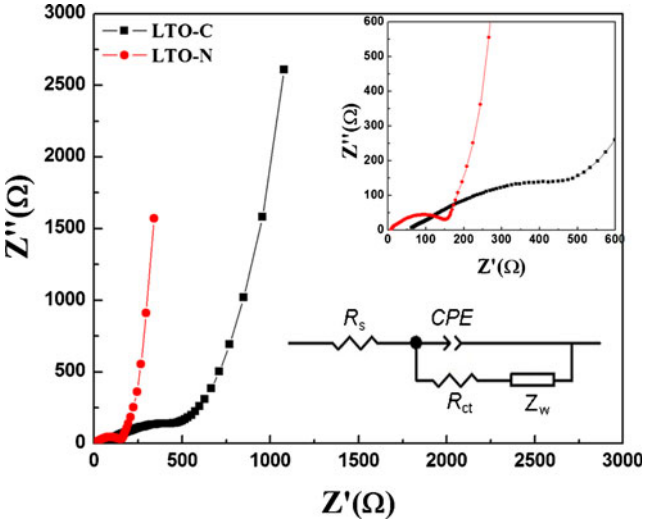

Fig. 5 Nyquist plots for LTO-C and LTO-N samples, as well as the equivalent circuit used to fit the EIS; the *top right inset* is the enlarged Nyquist plot

To deeply study the advantage of the nitridation treatment on the LTO material, the electrical conductivities of pyrolyzed carbon, nitrogen-doped carbon, and TiO_xN_y films are

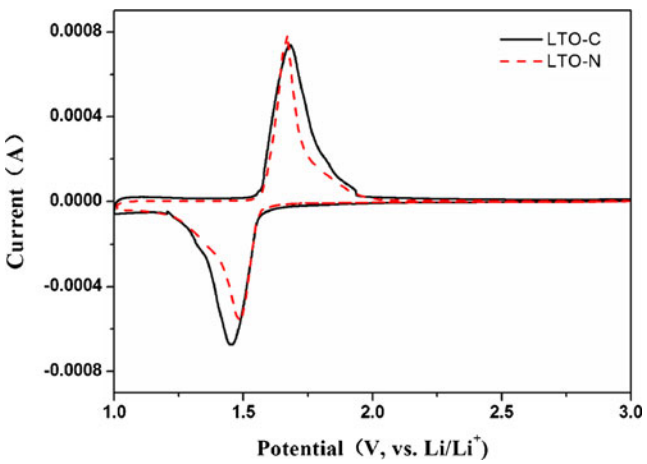

Fig. 4 Cyclic voltammograms of LTO-C and LTO-N between 1 and 3 V at a scan rate of 0.2 mVs^{-1}

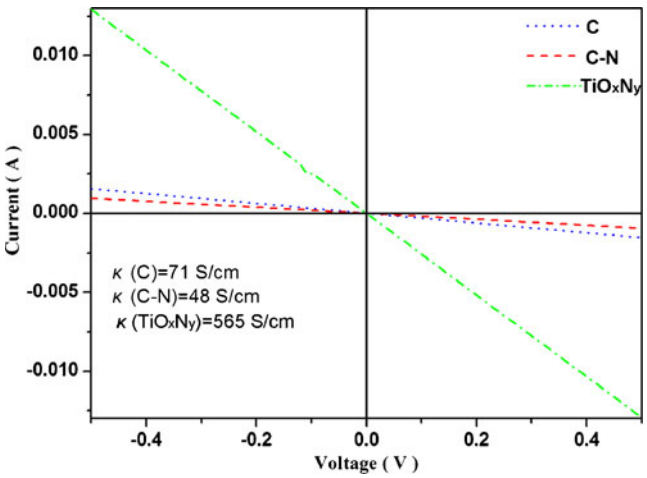

Fig. 6 Electrical conductivity test of 100-nm-thick pyrolyzed carbon, nitrogen-doped carbon, and TiO_xN_y films

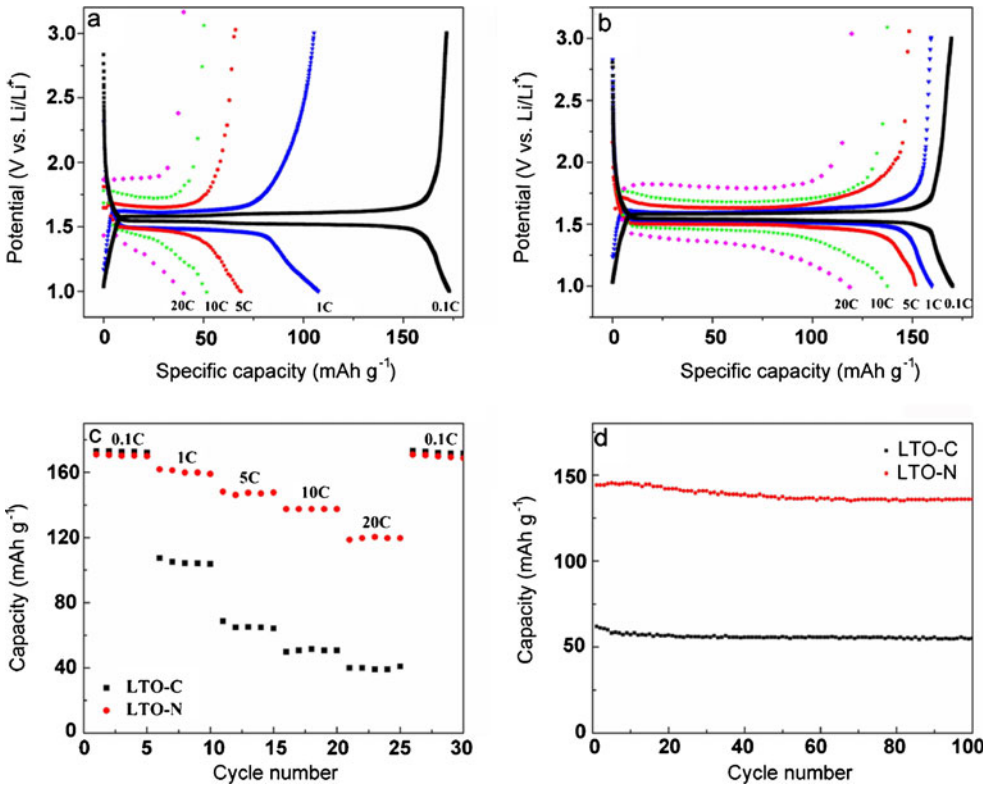

Fig. 7 **a** The discharge/charge curves of LTO-C at 0.1, 1, 5, 10, and 20 C. **b** The discharge/charge curves of LTO-N at 0.1, 1, 5, 10, and 20 C. **c** Cycling performance of LTO-C and LTO-N at different rates. **d** Cycling performance of LTO-C and LTO-N at 10 C

compared as shown in Fig. 6. The thickness of these films is measured by Veeco Dektak 150, and the electrical conductivity is conducted by Keithley 2440 5A source meter. The pyrolyzed carbon film was prepared by a pyrolysis process (thermally annealed at 800 °C in N_2 atmosphere) of the PEG 20000 film, which was spin coated from an ethanol solution on quartz substrates. According to the formulas $R=U/I$, $G=1/R$, and $G=\kappa A/l$ and test result in Fig. 6, it is calculated that its conductivity is ~71 Scm^{-1}. After a high-temperature ammonia treatment at 700 °C for 1 h, the carbon film was transformed to nitrogen-doped carbon with a conductivity decreased to 48 Scm^{-1}. TiO_xN_y film was prepared by annealing of TiO_2 sol film firstly at 500 °C in air and then in ammonia atmosphere at 700 °C for 1 h, which is similar to the thermal nitridation process of LTO. It is measured that the conductivity of TiO_xN_y films is up to 565 Scm^{-1}, which is more than ten times higher than that of the nitrogen-doped carbon films. Thus, we propose that the alleviated polarization (Fig. 5) and decreased R_{ct} (Fig. 6) mostly are attributed to the formation of highly conductive thin TiO_xN_y layer on the surface of the nanoparticles, indicating its huge potential on the enhancement of rate capability of the LTO material.

Figure 7 evaluates the galvanostatic charge and discharge voltage profiles and specific capacities of LTO-C and LTO-N samples at different rates between 1.0 and 3.0 V voltage limits. At different current rates of 0.1, 1, 5, 10, and 20 C, the LTO-C (Fig. 7a) shows reversible capacities of 173, 107, 70, 52, and 40 $mAhg^{-1}$, respectively, while after a subsequent thermal nitridation treatment, those capacities increase to 170, 160, 152, 138, and 120 $mAhg^{-1}$, respectively, as Fig. 7b reveals (1 C means insertion of 3 mol Li into $Li_4Ti_5O_{12}$ in 1 h). It can be seen clearly that the polarization between the discharge and charge plateaus for the LTO-N sample is significantly lower compared to the LTO-C sample, especially at high current rates, indicating that the kinetic of the LTO sample is indeed improved after nitridation. As shown in Fig. 7c, at a low current rate of 0.1 C, both the LTO-C and LTO-N samples reach nearly the same discharge capacities. Whereas, the capacities of LTO-N at high current rates are much higher than those of LTO-C; particularly, the capacities of LTO-N are twice higher than those of LTO-C at 20 C. Such performance is better than the previously reported nitrogen-doped LTO derived from nitrogen-based organic precursors as the nitrogen source, such as ionic liquids, urea, and pyridine [25, 26, 28]. Table S5 in the supporting information makes comparisons of rate performance for LTO-N synthesized in this work with N-doped $Li_4Ti_5O_{12}$ reported in other literatures. Better performance of our LTO-N indicates the benefit of the gas-phase nitridation to form a conductive TiO_xN_y layer on the mesoporous LTO spheres. Figure 7d shows that the initial capacity of LTO-N reaches 144 $mAhg^{-1}$ at 10 C, which slightly decreases to 136 $mAhg^{-1}$ after 100 cycles with a capacity retention of 94 %. However, for the LTO-C sample, the initial capacity at 10 C is only 77 $mAhg^{-1}$ and decreases to 62 $mAhg^{-1}$ after 100 cycles with capacity retention of 80 %. It is considered that such outstanding rate and cycling

performance are mainly caused by a favorable interface generated by conductive TiO_xN_y nanolayer at the surface of LTO and highly efficient mixed network. Therefore, this unique nanostructure endows a synergistic effect of electrons transport and lithium-ion diffusion for realization of fast charging and discharging, which is very beneficial for the high-power lithium-ion batteries.

Conclusion

In conclusion, nitridated mesoporous LTO spheres were prepared by a simple ammonia treatment method. Homogenous TiO_xN_y layer was in situ constructed on the primary LTO nanoparticles' surface. This outstanding rate and cycling performance are caused by the favorable interface and three-dimensional efficient mixed network generated by more conductive TiO_xN_y layer and nitrogen-doped carbon at the surface of LTO. Such design also can be versatile for lithium-ion batteries materials to achieve the fast charging and discharging, which is very beneficial for the high-power applications.

Acknowledgments We appreciate the support of the "100 Talents" program of the Chinese Academy of Sciences, National Program on Key Basic Research Project of China (973 Program) (no. MOST2011CB935700), the National Natural Science Foundation (grant nos. 21271180, 21275151, 51202266, and 51272113), and the Qingdao Key Lab of solar energy utilization and energy storage technology.

References

1. Tarascon JM, Armand M (2001) Nature 414:359–367
2. Choi NS, Chen Z, Freunberger SA, Ji X, Sun YK, Amine K, Yushin G, Nazar LF, Cho J, Bruce PG (2012) Angew Chem Int Ed 51:9994–10024
3. Zhu GN, Wang YG, Xia YY (2012) Energy Environ Sci 5:6652–6667
4. Yoshio M, Wang HY, Fukuda K, Umeno T, Abe T, Ogumi Z (2004) J Mater Chem 14:1754–1758
5. Shen LF, Yuan CZ, Luo HJ, Zhang XG, Chen L, Li HS (2011) J Mater Chem 21:14414–14416
6. Shen L, Yuan C, Luo H, Zhang X, Xu K, Zhang F (2011) J Mater Chem 21:761–767
7. Wang YQ, Guo L, Guo YG, Li H, He XQ, Tsukimoto S, Ikuhara Y, Wan LJ (2012) J Am Chem Soc 134:7874–7879
8. Wagemaker M, van Eck ERH, Kentgens APM, Mulder FM (2008) J Phys Chem B 113:224–230
9. Yi TF, Xie Y, Wu Q, Liu H, Jiang L, Ye M, Zhu R (2012) J Power Sources 214:220–226
10. Cai R, Yu X, Liu XQ, Shao ZP (2010) J Power Sources 195:8244–8250
11. Yi TF, Xie Y, Jiang LJ, Shu J, Yue CB, Zhou AN, Ye MF (2012) RSC Adv 2:3541–3547
12. Liu Z, Zhang N, Sun K (2012) J Mater Chem 22:11688–11693
13. Jiang C, Ichihara M, Honma I, Zhou H (2007) Electrochim Acta 52:6470–6475
14. Lin YS, Tsai MC, Duh JG (2012) J Power Sources 214:314–318
15. Arico AS, Bruce P, Scrosati B, Tarascon JM, van Schalkwijk W (2005) Nat Mater 4:366–377
16. Li J, Tang Z, Zhang Z (2005) Electrochem Commun 7:894–899
17. Wen Z, Yang X, Huang S (2007) J Power Sources 174:1041–1045
18. Huang S, Wen Z, Zhang J, Yang X (2007) Electrochim Acta 52:3704–3708
19. Guo X, Wang C, Chen M, Wang J, Zheng J (2012) J Power Sources 214:107–112
20. Li H, Zhou H (2012) Chem Commun 48:1201–1217
21. Zhu GN, Liu HJ, Zhuang JH, Wang CX, Wang YG, Xia YY (2011) Energy Environ Sci 4:4016–4022
22. Jung HG, Myung ST, Yoon CS, Son SB, Oh KH, Amine K, Scrosati B, Sun YK (2011) Energy Environ Sci 4:1345–1351
23. Tang Y, Yang L, Qiu Z, Huang J (2009) J Mater Chem 19:5980–5984
24. Shen L, Yuan C, Luo H, Zhang X, Xu K, Xia Y (2010) J Mater Chem 20:6998–7004
25. Zhao L, Hu YS, Li H, Wang Z, Chen L (2011) Adv Mater 23:1385–1388
26. Pan H, Zhao L, Hu YS, Li H, Chen L (2012) Chem Sus Chem 5:526–529
27. Dong S, Chen X, Gu L, Zhou X, Xu H, Wang H, Liu Z, Han P, Yao J, Wang L, Cui G, Chen L (2010) ACS Appl Mater Interf 3:93–98
28. Park KS, Benayad A, Kang DJ, Doo SG (2008) J Am Chem Soc 130:14930–14931
29. Drygas M, Czosnek C, Paine RT, Janik JF (2006) Chem Mater 18:3122–3129
30. Etacheri V, Seery MK, Hinder SJ, Pillai SC (2010) Chem Mater 22:3843–3853
31. Gicquel A, Laidani N, Saillard P (1990) Pure Appl Chem 62:1743–1750
32. Zhong LS, Hu JS, Wan LJ, Song WG (2008) Chem Commun 10:1184–1186
33. Wan Z, Cai R, Jiang S, Shao Z (2012) J Mater Chem 22:17773–17781
34. Ding Z, Zhao L, Suo L, Jiao Y, Meng S, Hu YS, Wang Z, Chen L (2011) Phys Chem Chem Phys 13:15127–15133
35. Wang Y, Liu H, Wang K, Eiji H, Wang Y, Zhou H (2009) J Mater Chem 19:6789–6795
36. Zhang K, Wang H, He X, Liu Z, Wang L, Gu L, Xu H, Han P, Dong S, Zhang C, Yao J, Cui G, Chen L (2011) J Mater Chem 21:11916–11922
37. Zhang CJ, He X, Kong QS, Li H, Hu H, Wang HB, Gu L, Wang L, Cui GL, Chen LQ (2012) Cryst Eng Comm 14:4344–4349
38. Subramanian V, Zhu HW, Charan M, Kai-Hsuan H, Liu Z, Suenaga K, Wei BQ (2009) ACS Nano 3:2177–2184